# In vivo solid stress is associated with poor patient survival in glioma

Noah Jaitner<sup>1</sup>, Mehrgan Shahryari<sup>1,2</sup>, Jakob Schattenfroh<sup>1</sup>, Tom Meyer<sup>1</sup>, Hossein S. Aghamiry<sup>1</sup>, Jakob Ludwig<sup>1</sup>, Jakob Jordan<sup>1</sup>, Anastasia Janas<sup>2,3,4</sup>, Anna Morr<sup>1</sup>, Biru Huang<sup>1</sup>, Boshra Shams<sup>3,5</sup>, Thomas Picht<sup>3,5</sup>, Gueliz Acker<sup>3,4</sup>, Tobias Schaeffter<sup>6,7</sup>, Jing Guo<sup>1</sup>, Ingolf Sack<sup>1</sup>

<sup>1</sup>Department of Radiology, Charité – Universitätsmedizin Berlin, Germany

<sup>2</sup>Berlin Institute of Health at Charité – Universitätsmedizin Berlin, Germany

<sup>3</sup>Department of Neurosurgery, Charité – Universitätsmedizin Berlin, Germany

<sup>4</sup>Department of Radiation Oncology and Radiotherapy, Charité – Universitätsmedizin Berlin, Germany

<sup>5</sup>Cluster of Excellence: "Matters of Activity. Image Space Material", Humboldt University, Berlin, Germany

<sup>6</sup>Physikalisch-Technische Bundesanstalt, Berlin, Berlin, Germany

<sup>7</sup>Technical University Berlin, Einstein Center Digital Future, Berlin, Germany

# **Abstract**

Solid stress is increasingly being recognized as a key driver of tumor progression and aggressiveness, yet it has not been directly measured in patients so far. Here, we combine multifrequency magnetic resonance elastography with 3D magnetic resonance imaging (MRI)-based diffeomorphic deformable image registration network analysis to noninvasively quantify glioma-induced solid stress. In both a mouse model and patients, we identified spatially heterogeneous deformation patterns extending well beyond tumor margins. While deformation magnitude was not found to correlate with tumor size or clinical outcome, excess solid stress defined as the product of peritumoral volumetric strain and stiffness differential between unaffected brain and peritumoral tissue - was inversely associated with patient survival. To our knowledge, these findings provide the first in vivo indication that tumor-associated mechanical stress affects clinical outcomes and can thus serve as a quantitative, imaging-derived biomarker with potential utility for prognostication and treatment guidance in patients with glioma.

# Introduction

Gliomas are the most common malignant brain tumors with glioblastoma (GBM) being the most prevalent and lethal subtype, accounting for 54% of newly diagnosed gliomas<sup>1</sup>. GBM has a three-year survival rate of only 3-5% <sup>2</sup> and an incidence of 4.2 per 100,000 person-years <sup>3</sup>. Its poor prognosis is attributed to highly invasive growth, molecular heterogeneity, therapy resistance, and the lack of reliable imaging markers for differentiating true tumor progression from pseudoprogression<sup>4,5</sup>. There is an urgent need for robust imaging biomarkers to guide therapeutic decision-making and improve patient outcomes.

Understanding the biophysical and mechanical properties of gliomas, particularly in vivo, is essential, as these influence tumor-host interactions<sup>6</sup>, invasion<sup>7,8</sup>, and treatment response<sup>9,10</sup>. In vivo magnetic resonance elastography (MRE)<sup>11</sup> has revealed that gliomas exhibit unusual soft-solid properties compared to the typically highly viscous brain parenchyma<sup>12-15</sup>. This biomechanical signature has been suggested as a promoter of unstable physical boundary conditions and viscous fingering<sup>16</sup>. In contrast to most extracranial tumors, which share stiffer and more viscous properties than their surroundings, glioma present a reversed mechanical gradient which likely contributes to unique deformation patterns observed in peritumoral regions<sup>17</sup>. Radiomic analyses have consistently shown that peritumoral tissue in glioma exhibits large, heterogeneous deformation amplitudes<sup>18,19</sup>, indicating the accumulation of solid stress generated by the growing tumor. Solid stress – defined as the sum of mechanical shear and compressive forces acting on tissue<sup>20</sup> - has been suggested as a key driver of tumor aggressiveness by influencing cell signaling<sup>21</sup>, promoting cell unjamming<sup>22,23</sup>, and impairing perfusion through vascular compression<sup>24</sup>. Therefore, quantifying solid stress in vivo may provide critical insights into glioma progression and therapeutic resistance<sup>25</sup>.

However, directly measuring tumor solid stress in patients is difficult as spatially resolved force fields are typically inaccessible through non-invasive imaging techniques<sup>26-28</sup>. Nevertheless, nonlinear mechanical deformation models can predict solid stress by multiplying deformation with changes in elastic modulus<sup>29</sup>. Pioneering studies have assessed tumor-related deformation in patients with GBM using image registration to normative brain atlases<sup>19</sup>. However, these approaches lack critical information on the intrinsic mechanical properties of tissue, particularly the shear modulus, since deformation alone is insufficient to quantify solid stress<sup>27</sup>. Conversely,

isolated MRE measurement of glioma shear modulus offers limited predictive value for individual patient outcomes<sup>12, 30</sup>.

Therefore, we developed a method to quantify mechanical stress in peritumoral tissue induced by both volumetric and shear strain, through the combination of deformation and shear modulus measurements. We introduce a metric for tissue degradation, termed excess solid stress, derived from volumetric strain and the differential shear modulus between peritumoral regions and unaffected brain tissue. Our approach combines advanced multifrequency MRE with three-dimensional (3D) strain field analysis using diffeomorphic deformable image registration in patients with glioma. Following validation of 3D strain mapping in a longitudinal mouse model of GBM, we prospectively enrolled glioma patients for combined 3D MRI and MRE scanning. Excess solid stress was then evaluated to investigate its potential as a prognostic imaging biomarker of glioma aggressiveness, with respect to patient survival.

# Results

<u>Different registration methods consistently measure glioblastoma-induced displacement in mice</u>

Figure 1A presents the displacement fields obtained in two representative mice. There is strong outward displacement from the tumor into the surrounding brain. The direction of this displacement remained consistent whether the mouse brains were registered to a standard anatomical atlas or to reference time points. Tumors exhibited a mean volumetric increase of 863  $\pm$  100 % between time point 13 days and 22 days as previously analyzed  $^{31}$ . Tumor size at time point 22 days relative to the mouse brain atlas was  $34\pm20$ % (range: 12 % to 68 %). Figure 1B shows representative T2w images, displacement field magnitude, volumetric strain, and OSS maps of the brain of two mice for atlas and reference time point registration. For healthy control mice, mean displacement field magnitude was  $1.83\pm0.04\,mm$  with a 95th quantile of 3.22 mm. In contrast, GBM mice registered to the atlas exhibited a significantly higher mean displacement field magnitude of  $2.6\pm0.5\,mm$  compared to healthy controls (p < 0.001). For GBM mice registered to a reference time point at 13 days, the average displacement field magnitude was  $3.4\pm2.0\,mm$ . Regions exceeding the 95th percentile identified in healthy controls showed perimeter locations and size consistently across registrations to atlas and reference time point.

## Glioblastoma in mice induces volumetric strain

Group statistical analysis of normalized volumetric strain,  $\overline{tr(\mathbf{E})}$ , and normalized shear strain,  $\overline{OSS}$ , for healthy, atlas-registered GBM, and reference time point-registered GBM mice are shown in Figure 1C. In healthy control mice,  $\overline{tr(\mathbf{E})}$  was  $-0.0\pm0.5$ % while  $\overline{OSS}$  was  $0.0\pm0.7$ %. For atlas-registered GBM mice,  $\overline{tr(\mathbf{E})}$  was significantly lower than in healthy controls, both for unaffected brain regions ( $-9\pm1$ %, p < 0.001) and in peritumoral regions ( $-9\pm2$ %, p < 0.001).  $\overline{OSS}$  for atlas-registered GBM mice was  $0.7\pm1.1$ % for unaffected brain regions and  $-0.5\pm2.5$ % in peritumoral regions. Similarly, in reference time point-registered GBM mice,  $\overline{tr(\mathbf{E})}$  was significantly lower than in healthy controls for both unaffected brain regions ( $-5\pm2$ %, p < 0.001) and iperitumoral regions ( $-5\pm5$ %, p = 0.0098). In contrast,  $\overline{OSS}$  was similar in unaffected brain regions ( $-0.9\pm3.6$ %) and peritumoral regions ( $-0.3\pm4.0$ %), indicating that GBM in the mouse brain primarily induces volumetric strain rather than shear strain. Volumetric strain was lower when computed using atlas-based registration compared to the registration to a reference time point. The mean difference between the two registration methods was 3%, which we identify as a

systematic error associated with volumetric strain estimation. Conversely,  $\overline{OSS}$  did not differ significantly between atlas-based and reference time point-based registration.

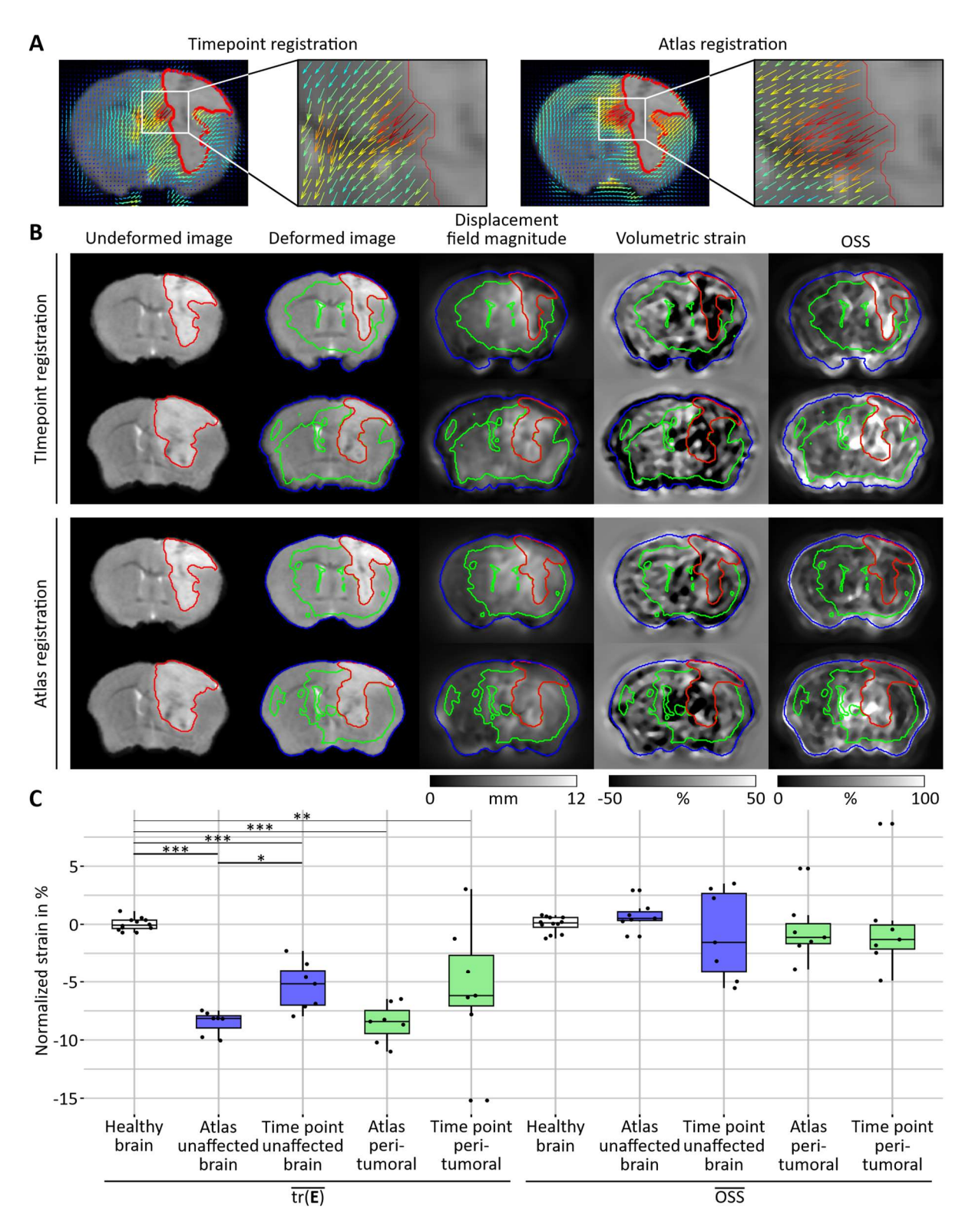


Figure 1 Results for in vivo mouse brain. (A) Representative displacement fields for two distinct mouse brains with magnified insets. The tumor region is outlined in red. (B) Results for two GBM mice with image registration to reference time point and to standardized atlas. Shown are the undeformed image, deformed image, displacement magnitude, volumetric strain, and OSS. Peritumoral regions with high displacement magnitude are outlined in green and unaffected regions in blue. (C) Group statistical analysis of normalized volumetric strain  $\overline{tr(E)}$  and normalized shear strain  $\overline{OSS}$  for

healthy mice, atlas-registered GBM mice, and reference time point registered GBM mice (green: peritumoral region, blue: unaffected brain region). \*p<0.05. \*\*p<0.01, \*\*\*p<0.001

#### Glioma in patients induces spatially heterogeneous peritumoral displacement fields

Figure 2A shows representative displacement fields obtained in two glioma patients. As highlighted in the insets, these fields reveal heterogeneously distributed areas of tissue displacement directed away from the tumor and exerted on the tumor-surrounding regions. Tumor size relative to the human brain atlas was  $1.5 \pm 1.5$ % (range: 0.2% to 5.8%), which was significantly smaller than in the mouse model (p < 0.001). Figure 2B presents T1w images, SWS maps, displacement field magnitude, volumetric strain, and OSS for the brains of two patients and two healthy volunteers. The magnitude of displacement in healthy volunteers was  $3.0 \pm 0.3$  mm, with a 95<sup>th</sup> percentile value of 6.5 mm. Henceforth the 95<sup>th</sup> percentile was taken as threshold for abnormal displacement in patients. Regions of abnormal displacement were heterogeneously distributed in the peritumoral regions of patients. No such regions were observed in healthy volunteers. Displacement magnitudes in non-tumor brain were significantly higher in glioma patients than in healthy volunteers (3.7  $\pm$  0.5 mm, p < 0.001).

#### Peritumoral regions are highly compressed and are softer than healthy tissue

Group statistical results for  $\overline{tr(\mathbf{E})}$ ,  $\overline{\text{OSS}}$ , and SWS and the corresponding regions are shown in Figure 3A and B, respectively.  $\overline{tr(\mathbf{E})}$  was highest, with a negative sign, in peritumoral regions, indicating compression  $(-17 \pm 9 \,\%)$ , followed by unaffected brain regions in patients  $(-9 \pm 5 \,\%)$ , p < 0.001) and healthy brains in volunteers  $(0 \pm 2 \,\%)$ , p < 0.001).  $\overline{\text{OSS}}$  was also highest in peritumoral regions  $(23 \pm 9 \,\%)$ , followed by unaffected brain regions in patients  $(13 \pm 6 \,\%)$ , p < 0.001) and healthy volunteers  $(0 \pm 2 \,\%)$ , p < 0.001). Mean SWS in healthy brain tissue was  $1.37 \pm 0.06 \,m/s$ , while SWS in unaffected brain regions  $(1.25 \pm 0.03 \,m/s)$ , p < 0.001) and peritumoral tissue of glioma patients  $(1.27 \pm 0.03 \,m/s)$ , p < 0.001) was significantly lower. Tumor SWS  $(1.21 \pm 0.07 \,m/s)$  was significantly lower than that of whole brain in healthy controls (p < 0.001), unaffected glioma brain (p = 0.038) and peritumoral regions (p = 0.007).

#### Degraded (softer) peritumoral tissue is highly deformed

Figure 3C shows that shear modulus in peritumoral tissue ( $\mu_1$ ) increased with volumetric strain in peritumoral regions, because  $\overline{tr(\mathbf{E})} < 0$  in all patients, consistently indicating compression. (slope:  $0.5 \pm 0.2$  kPa, intercept:  $1.71 \pm 0.03$  kPa, R = 0.55, p = 0.009). Further, peritumoral shear modulus  $\mu_1$  linearly decreased with shear strain  $\overline{OSS}$ , which, by definition, is always positive (slope:  $-0.5 \pm 0.2$  kPa, intercept:  $1.75 \pm 0.04$  kPa, R = -0.60, p = 0.004). Thus, larger strain, both volumetric and shear, was associated with softer tissue properties as a sign of deformation-induced degradation of peritumoral tissue. Combined assessment of strain and shear modulus enabled us to determine in vivo solid stress,  $\sigma = \sigma_{vol} + \sigma_{shear}$ , according to equations (10) and (11). Assuming a Poisson's ratio of v = 0.4 according to Moran et al.<sup>32</sup> (see Methods), volumetric solid stress  $\sigma_{vol}$  was  $1.2 \pm 0.6$  kPa with a range of  $2.2 \pm 0.2$  kPa to  $0.1 \pm 0.2$  Pa. Significantly lower values were found for shear stress  $\sigma_{shear}$  with  $0.7 \pm 0.3$  kPa and ranges of  $1.1 \pm 0.2$  kPa to  $0.3 \pm 0.1$  kPa (p < 0.001).

#### Highly deformed peritumoral tissue is stiffer than apparently unaffected tissue

Although we observed tissue degradation and softer values of  $\mu_1$  in conjunction with higher strain magnitudes in peritumoral regions, differential modulus  $\Delta\mu=\mu_0-\mu_1$  showed the opposite trend of lower values at higher strain, both volumetric (slope:  $-0.6\pm0.2~m/s$ , intercept:  $-0.16\pm0.04~m/s$ , R = -0.56, p = 0.008) and shear (slope:  $0.7\pm0.2~m/s$ , intercept:  $-0.21\pm0.05~m/s$ , R =

0.63, p = 0.002, Figure 4A). This observation strongly indicates that the whole brain is mechanically altered when glioma-induced tissue compression occurs.

#### Excess solid stress in GBM has prognostic value

Since  $\Delta\mu$  reflects differential stiffness - and thus local (peritumoral) and global tissue (unaffected brain) degradation - we further investigated the prognostic value of excess solid stress, defined as the product of  $\Delta\mu$  and strain according to equations (12) and potentially representing the mechanical driver of degradation. To this end, we analyzed a subgroup of 10 patients (1 WHO grade II, 1 WHO grade III, and 8 WHO grade IV) for whom survival data were available (Mean: 836  $\pm$  466 days, range: 162 to 1514 days). Excess solid stress  $\Sigma_{vol}$  showed a significant linear decline with length of survival (slope:  $-0.017 \pm 0.006 \, Pa/days$ , intercept:  $-19 \pm 6 \, Pa$ , R = -0.70, p = 0.02, Figure 4B). Mean  $\Sigma_{vol}$  was  $4.3 \pm 11.6 \, Pa$ , ranging from  $30 \pm 7 \, Pa$  to  $-13 \pm 6 \, Pa$ . Excess solid stress did not correlate with tumor size or WHO grade, due to the limited sample size of grade II and III tumors. Mean  $\Sigma_{shea}$  was  $-7.2 \pm 14.2 \, Pa$ , ranging from  $16 \pm 65 \, Pa$  to  $-31 \pm 70 \, Pa$ . In line with our solid stress analysis, which demonstrated that  $\sigma_{vol}$  was approximately twice as high as  $\sigma_{shear}$ , the prognostic relevance of  $\Sigma_{vol}$  exceeded that of  $\Sigma_{shear}$  (p = 0.13). Preoperative Karnofsky performance status scale and Aachen Aphasia Test $^{33}$  results revealed no significant impairment in 8 of the 10 patients, suggesting no direct correlation between mechanical stress and survival in this subset.

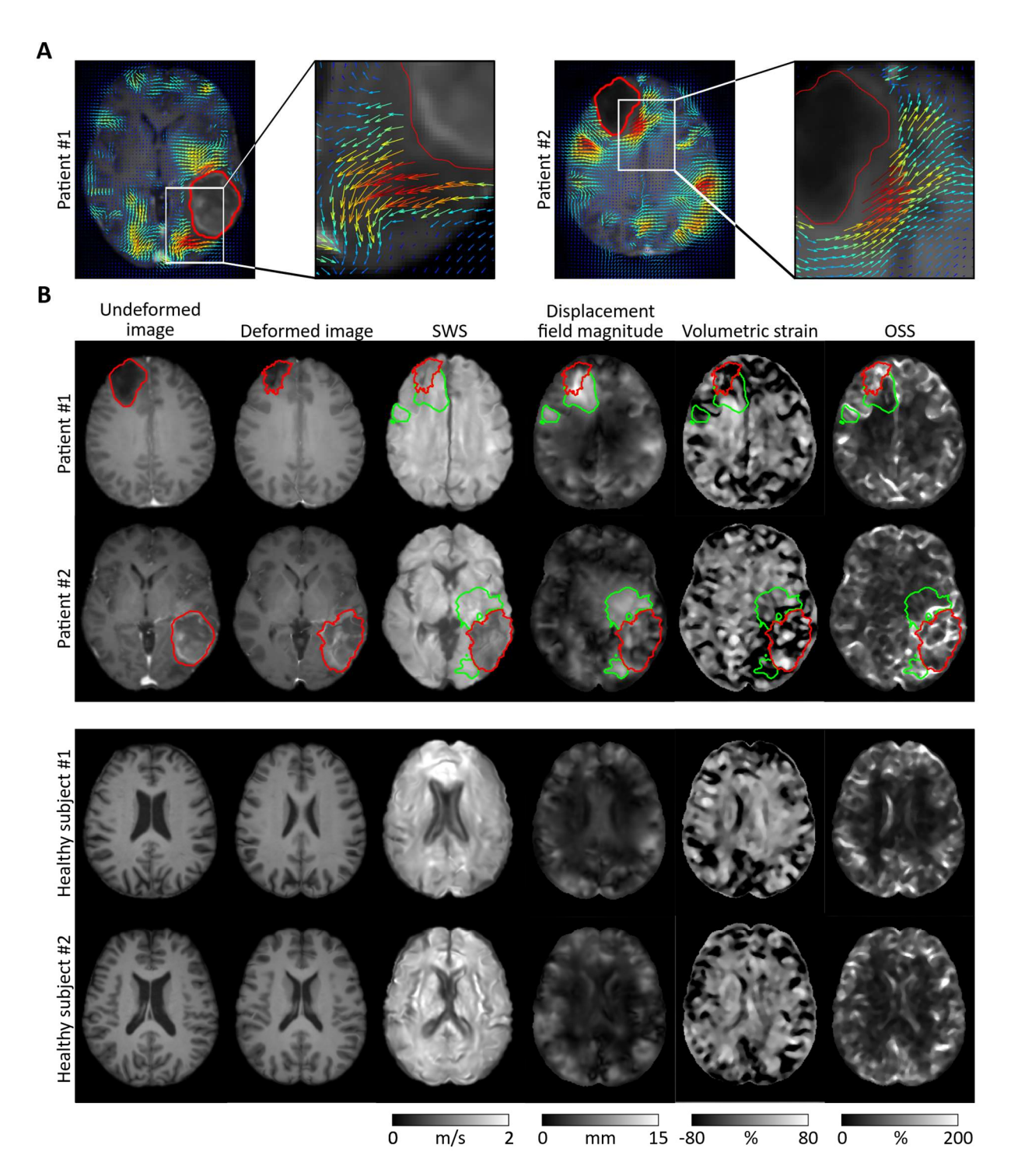


Figure 2 Representative result maps illustrating findings in glioma patients and healthy controls. (A) Displacement fields in a central axial slice from two patients with glioma. Tumor boundaries are outlined in red; magnified views highlight regional deformation. (B) Image registration outputs for two glioma patients and two healthy controls, including undeformed/deformed images, displacement magnitude, volumetric strain, and OSS. Peritumoral regions exhibiting abnormally increased displacement magnitudes are outlined in green; tumor margins are shown in red.

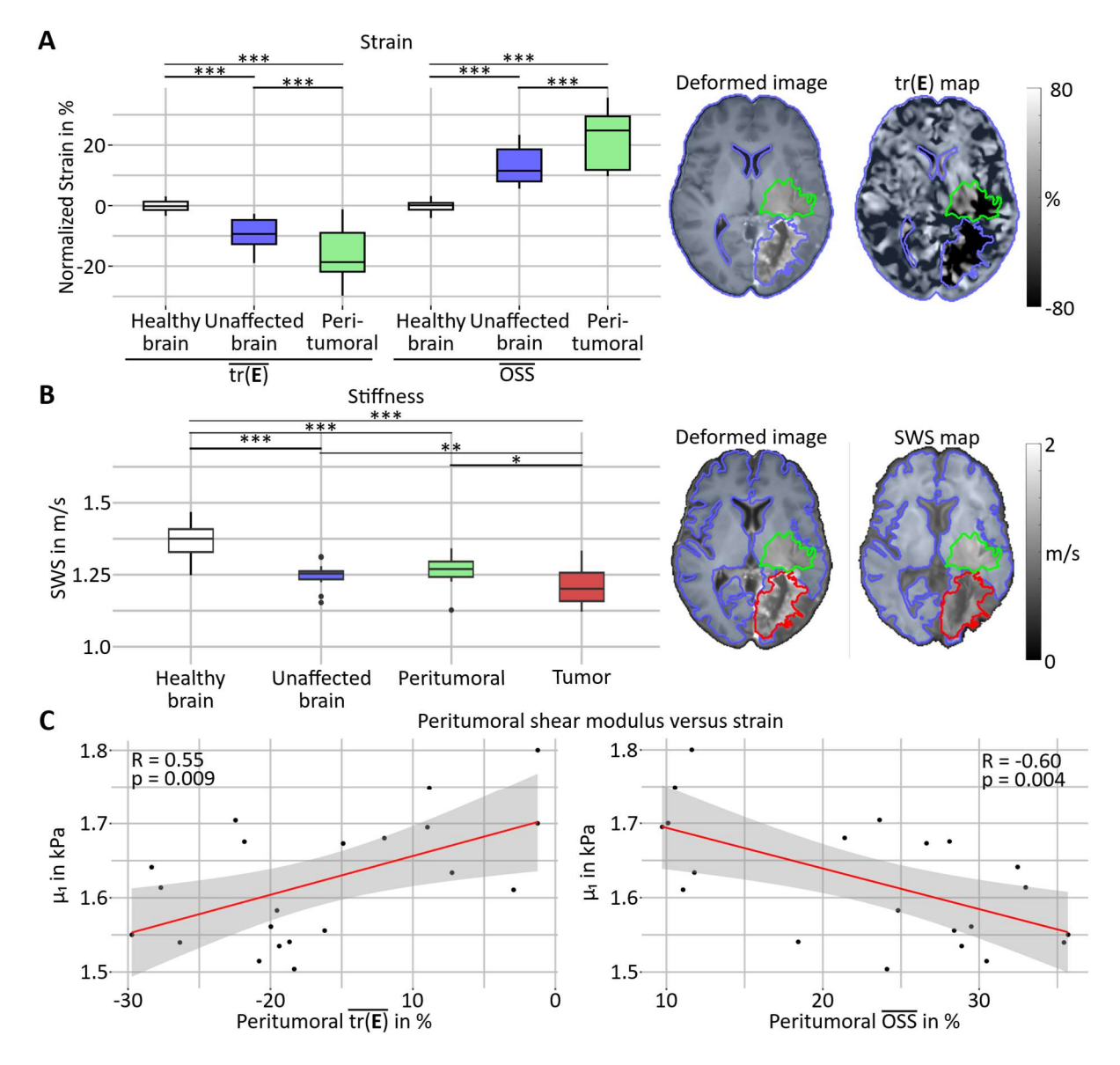


Figure 3 Group statistical results for human subjects. (A) Group comparisons of normalized volumetric strain  $\overline{tr(E)}$  and  $\overline{OSS}$  between glioma patients and healthy controls across defined regions (green: peritumoral area, blue: unaffected brain region without tumor). (B) Group comparisons of SWS across glioma patients and controls, averaged over green (peritumoral), red (tumor), and blue (unaffected) regions as indicated. (C) Scatter plot of peritumoral shear modulus  $\mu_1$  versus normalized volumetric strain  $\overline{tr(E)}$  and  $\overline{OSS}$  across glioma patients. Linear regression revealed increasing peritumoral shear modulus with normalized volumetric strain  $\overline{tr(E)}$  (slope:  $0.5 \pm 0.2$  kPa, intercept:  $1.71 \pm 0.03$  kPa, R = 0.55, p = 0.009) and decreasing with  $\overline{OSS}$  (slope:  $-0.5 \pm 0.2$  kPa, intercept:  $1.75 \pm 0.04$  kPa, R = -0.60, p = 0.004). \*p<0.05. \*\*p<0.01, \*\*\*p<0.001

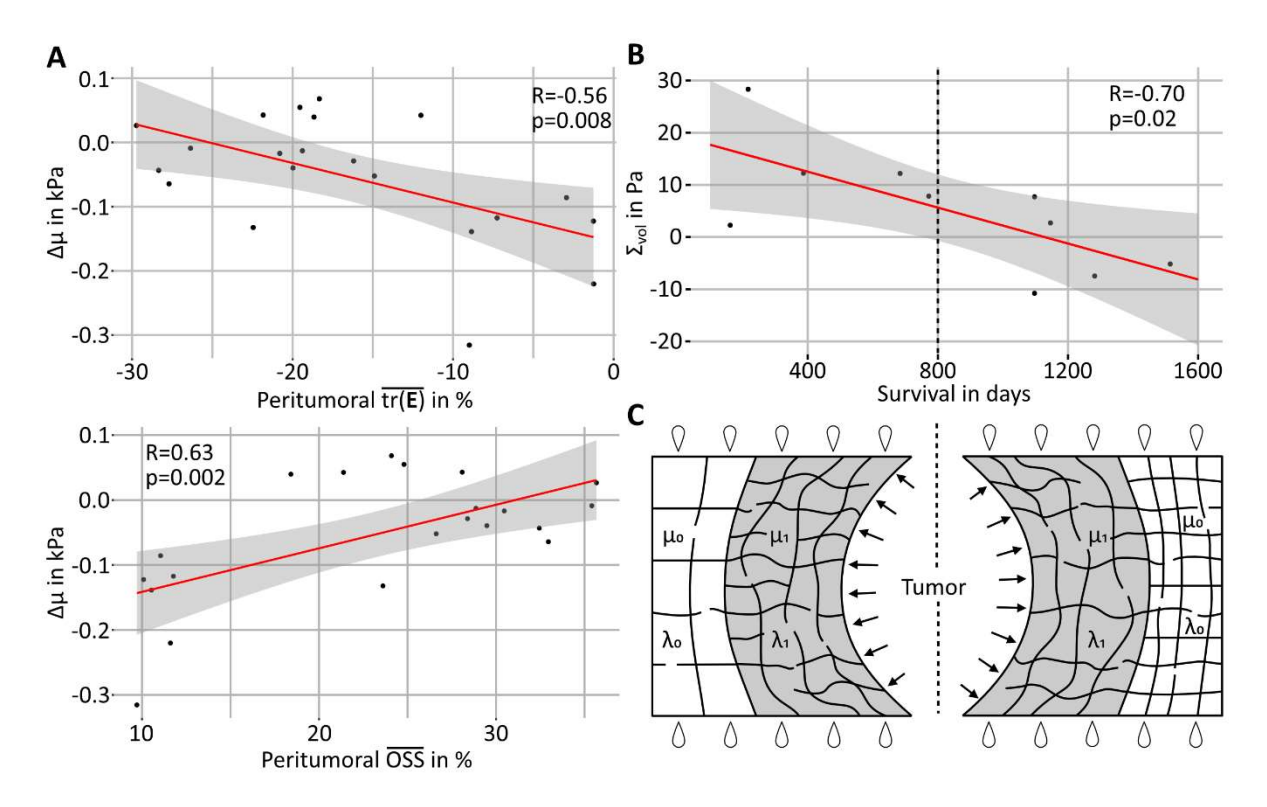


Figure 4 Group statistical results for patients with glioma and mechanical alterations in peritumoral brain tissue. (A) Scatter plot of differential shear modulus  $\Delta\mu$  versus normalized volumetric strain  $\overline{tr(E)}$  and  $\overline{OSS}$  across patients. Linear regression revealed decreasing differential shear modulus  $\Delta\mu = \mu_0 - \mu_1$  with normalized volumetric strain  $\overline{tr(E)}$  (slope:  $-0.6 \pm 0.2$  m/s, intercept:  $-0.16 \pm 0.04$  m/s, R = -0.56, p = 0.008) and increasing with  $\overline{OSS}$  (slope:  $0.7 \pm 0.2$  m/s, intercept:  $-0.21 \pm 0.05$  m/s, R = 0.63, p = 0.002). (B) Excess volumetric stress  $\Sigma_{vol}$  plotted against patient survival. A negative correlation was observed (slope =  $-0.017 \pm 0.006$  Pa/days, intercept =  $19 \pm 6$  Pa, R = -0.7, p = 0.02), suggesting that lower excess stress improves survival. (C) Schematic illustration of mechanical processes in brain tissue during tumor progression. The peritumoral region is shown in gray. As the tumor expands, it exerts stress on the surrounding tissue, promoting interstitial fluid drainage and tissue degradation. Throughout this process, the first Lamé parameter ( $\lambda_0 = \lambda_1$ ) remains effectively constant, consistent with the tissue's near-incompressibility<sup>29</sup>. In contrast, shear modulus  $\mu$  increases in response to compression stiffening<sup>21</sup> or decreases in response to tissue degradation<sup>34</sup>. On the left, the peritumoral region is stiffer compared to unaffected tissue ( $\mu_1 > \mu_0, \Sigma_{vol} > 0$ ), while, on the right, this trend is reversed ( $\mu_0 > \mu_1, \Sigma_{vol} < 0$ ). Stiffer healthy (unaffected) tissue relative to the peritumoral region is associated with a better patient prognosis, as indicated by the dotted line.

# Discussion

Our study conceptually merges two previously distinct MRI-based approaches, 3D deformation analysis and stiffness mapping, to measure mechanical stress in glioma patients. The novel biomarker, excess stress, integrates cause and consequence of brain tissue degradation from a biomechanical perspective, that is, large deformation and intrinsic softening. Probably for this reason, elevated excess stress correlates with shorter patient survival, suggesting a potential mechanobiological link to glioma aggressiveness and therapeutic responsiveness.

The peritumoral region in glioma is a complex and dynamic microenvironment, characterized by the interplay of cellular and extracellular components that contribute to tumor growth, invasion, and resistance to therapy<sup>6, 35</sup>. GBM exhibits highly infiltrative and irregular growth patterns with striking capacities to establish a brain-wide neuronal circuit connectome<sup>7</sup>. This highly invasive behavior results in substantial displacement of brain tissue with a gradient from high deformation magnitudes to subtle displacements invisible on a coarse MRI grid<sup>36-38</sup>. Areas exhibiting high deformation magnitudes are heterogeneously distributed around the tumor core, extending deep into apparently healthy brain tissue. These observations are consistent with prior studies

demonstrating that glioma infiltration is facilitated in mechanically heterogeneous environments, where stiffness gradients contribute to tumor progression<sup>6,39</sup>. In our study, the peritumoral region consistently exhibited higher volumetric strain compared to apparently unaffected brain matter in both mice and humans, indicating the dominating compression force exerted by the tumor. In contrast, shear deformation measured by OSS was significantly elevated only in patients but not in mice, suggesting that GBM grows less invasively in the mouse model than in the human brain. Consistently, volumetric strain was significantly lower in mice than in patients despite relatively larger tumor size (approximately 56% larger tumors relative to the full brain volume in mice than in human). This difference suggests that tissue replacement rather than displacement occurs during tumor progression in the mouse model.

The observed positive correlation between shear modulus and volumetric strain in glioma patients indicates that mechanically softer peritumoral regions undergo greater compression (larger negative volumetric strain) than their stiffer counterparts. This finding could be explained by chronic compression leading to brain tissue degradation and softening, similar to pressure peaks observed in patients with hydrocephalus, which result in lower brain stiffness<sup>40</sup>. Notably, this compression-induced brain softening arises from large strains acting on the tissue over weeks, months, or years of tumor development and causes tissue-degrading mechanical stress. In contrast, *compression stiffening* of brain tissue, as reported by Janmey and colleagues<sup>21</sup>, describes a short-term hyperelastic stiffness response of *intact* tissue.

Rather than hyperelastic stiffening, we observed softening in both peritumoral and unaffected brain tissue of glioma patients compared to healthy volunteers. This finding is consistent with previous reports of glioma-associated tissue remodeling and structural degradation far beyond the tumor margins, reflecting a diffuse, whole-brain process<sup>41-43</sup>. In our study, patients with stiffer peritumoral regions compared to unaffected tissue ( $\mu_0 < \mu_1$ ) had positive excess volumetric stress ( $\Sigma_{vol} > 0$ ) and shorter survival than patients where this trend was reversed ( $\mu_0 > \mu_1, \Sigma_{vol} < 0$ 0 ). Therefore, differential stiffness  $\Delta\mu$  between large-strain (peritumoral) and low-strain (apparently unaffected) tissue seems to be a key parameter of GBM biomechanics. Neither the size of large-strain regions or the tumor, nor any stiffness parameter of tumor or peritumoral region (all being softer than healthy brain tissue) correlated with length of survival. A possible explanation of the sensitivity of solid-stress related biomechanics to glioma survival is the interplay between tissue degradation and residual compression stiffening. Patients with widespread degradation (low  $\mu_0$ ) in apparently unaffected brain matter and highly deformed peritumoral tissue (higher  $\mu_1$ ) fall into the poor-prognosis group irrespective of which of the two regions contributes most to this unfavorable scenario. Vice versa, patients with intact global brain matter mechanistically benefit from higher  $\mu_0$  values and more favorable biomechanical scenarios. Our method is the first which discriminates between pre-stressed intact and degraded tissue and quantifies tissue integrity versus degradation using the combined strain-stiffness parameter of excess volumetric stress.

Comparing our results with the literature, we note that our healthy brain stiffness values fall in the range of previously reported values  $^{44, 45}$ . Furthermore, our findings agree with earlier work demonstrating that tumor tissue is softer than surrounding healthy tissue  $^{12, 30}$ . Peritumoral regions have not consistently been found to demonstrate stiffening compared to healthy surrounding tissue. Nia et al.  $^{26}$  reported ex vivo radial solid stress values of approximately 20 Pa in GBM using a planar-cut method following tissue embedding in agarose, while in situ estimates based on a needle-biopsy technique coupled with a mathematical model yielded circumferential stress values around 100 Pa. Intraoperative estimates fell into the range of 10 to 600 Pa  $^{46}$ . The shear stress values obtained in our study fall within a similar range. However, the volumetric solid stress values we report are higher, possibly due to differences in methodology and physiological

context. A critical parameter in solid stress estimation is the Poisson's ratio, which is not directly measurable in vivo and thus relies on modeling assumptions. Nia et al. employed a relatively low value ( $\nu=0.1$ ), whereas we adopted a higher value ( $\nu=0.4$ ), which is closer to the near-incompressibility of brain tissue used in standard models³². In incompressible materials, volumetric deformation would require infinite stress, which is unphysical. This highlights the limitations of modeling brain tissue as an elastic solid over longer time periods, where a growing tumor acts as fluid-like mass source ⁴7. In an unjacked poroelastic scenario, fluid outflow from the tissue surrounding a growing tumor mass mitigates pressure buildup and relaxes volumetric stress. Moreover, GBM not only displaces brain tissue but also gradually replaces it, altering its local mechanical properties and degrading tissue structure.

Although encouraging, our study has limitations. First, the sample size is relatively small and homogeneous, particularly for the analysis of clinical prognosis. Therefore, validation in larger, more heterogeneous populations will be essential to substantiate our findings. Second, our methodology depends on image registration to a standardized brain atlas, which may introduce inaccuracies, particularly in individuals with anatomical deviations from standard brain anatomy. To partially account for this, we included healthy controls and adjusted for the effects of deviant brain anatomy on our displacement measurements. Thirdly, despite the use of diffeomorphic registration techniques, the reliance on image contrast may result in misalignments as underlying mechanical properties are not taken into consideration. Future work could address this by incorporating physics-informed registration frameworks that implement stiffness measurements directly into strain estimation. Lastly, in our estimation of volumetric solid stress, we adopted a Poisson's ratio based on values reported in other studies<sup>32</sup>. Performing a joint estimation of the Lamé parameters alongside volumetric stress might allow a more precise quantification of solid stress.

In summary in this study, we present a novel, noninvasive method to quantify volumetric and shear stress in patients with glioma and a mouse GBM model, leveraging deformation mapping and MRE towards prognostic assessment of excess volumetric stress. We demonstrate that high volumetric compression - particularly in softer, compliant brain regions - extends into healthy tissue, indicating heterogeneous stress distributions that mirror glioma infiltration patterns. Our findings demonstrate the significance of mechanical stress as a critical, quantifiable MRI biomarker of glioma pathophysiology and underscore its potential for diagnosis and therapy monitoring.

# Methods

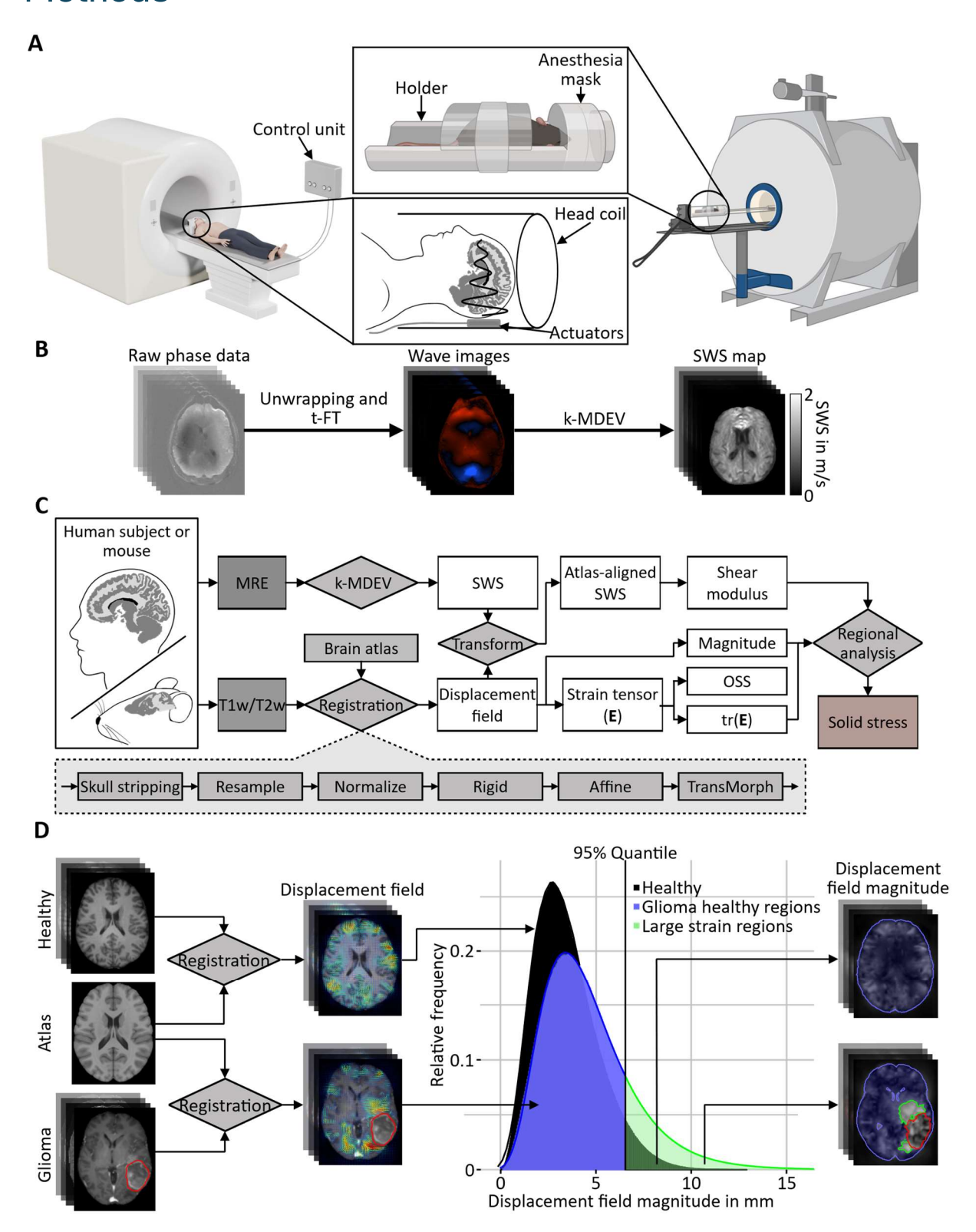


Figure 5 Pipeline for the acquisition and analysis of magnetic resonance elastography (MRE) and 3D magnetic resonance imaging (MRI) data in humans and mice. (A) Experimental setup. In human subjects, MRE and 3D-MRI were performed using a 3T clinical MRI scanner at a single time point. Multifrequency MRE vibrations were excited using two compressed-air-powered actuators placed beneath the head. In mice, T2-weighted (T2w) MRI was performed at two time points during tumor progression. Mice were secured in a holder and scanned in a 7T preclinical MRI system. (B) Postprocessing steps of MRE. Raw phase data is first unwrapped, followed by a temporal Fourier transform (t-FT) to extract the fundamental of angular drive frequency  $\omega$ . The resulting wave images are then inverted according to equations (1) and (2) using k multifrequency dual elasto-visco inversion (k-MDEV). (C) Analysis workflow. Human T1-

weighted (T1w) and mouse T2w images, along with corresponding MRE data for humans, were processed. MRE data were inverted using the k-MDEV algorithm to generate shear wave speed (SWS) maps. Anatomical images were registered to species-specific atlases (MNI ICBM Human Brain Atlas<sup>48</sup>; DSURQE Mouse Brain Atlas<sup>49</sup>) by skull stripping, resampling, normalization, rigid and affine transformations, and deformable registration using a transformer-based model. Resulting deformation fields were used to align SWS maps of humans, and the shear modulus was computed. Strain tensors derived from displacement fields enabled calculation of displacement magnitude, volumetric strain (tr(E)), and octahedral shear strain (OSS) according to equations (5), (7a) and (7b). Regions with elevated displacement magnitudes were used to estimate stress (equations (10)-(12)). (D) Regional analysis. Displacement magnitudes were quantified following registration. Histogram analysis was used to compare values across healthy subjects and glioma patients. Regions exceeding the 95th percentile of displacement magnitudes in unaffected tissue were identified and are visualized in green.

# Study Design

Seven female C57BL/6 mice ( $10 \pm 2$  weeks old) were investigated at 13 and 22 days following GBM implantation as previously published in Janas et al.<sup>31</sup>. An additional group of twelve female C57BL/6 mice (12 weeks old) were used as healthy controls. All animal experiments followed German animal protection law and were monitored by local authorities (LaGeSo, Berlin, Germany, registration numbers G0130/20 and G0284/ $13^{31,50}$ ). Clinical MRI and MRE was performed in twenty-one patients with glioma prior to surgical resection (6 women,  $52 \pm 12$  years, 2 WHO Grade II, 2 WHO Grade III, 17 WHO Grade IV) and 16 healthy volunteers (4 women,  $45 \pm 13$  years, age range: 28 to 60 years). The study was approved by the internal review board of Charité - Universitätsmedizin Berlin (EA1/248/19). Written informed consent was obtained from all participants.

## Specimen preparation

Tumor cell implantation was performed as previously described  $^{31,\,51}$ . In brief, anesthetized mice were placed in a fixation frame, and the skull was exposed. An injection of 20,000 GL261 tumor cells was administered into the right striatum (2 mm lateral, 1 mm anterior, and 3 mm deep from the bregma) using a 1  $\mu$ L Hamilton syringe over a 15-minute period. Mice were anesthetized with ketamine/xylazine (ketamine-hydrochloride + 1 mg xylazine per 100 g bodyweight) during the procedure.

#### **Imaging**

#### Volumetric MRI in mice

Imaging was performed on a preclinical 7T MRI scanner (BioSpec 70/20 USR, Bruker, Germany and Paravision 6.0.1 Software) using a 20-mm diameter volume coil (RAPID Biomedical, Rimpar, Germany). The mice were anesthetized with isoflurane (1.0–1.5%, CP Pharma, Burgdorf, Germany) diluted in a mixture of 30% O2 and 70% N2O and placed inside the scanner (see Figure 5A). To assess tumor volume in GBM-bearing mice, 32 contiguous axial image slices were acquired using a T2-weighted (T2w) rapid acquisition with refocused echoes (RARE) sequence (repetition time (TR) = 4200 ms, echo time (TE) = 36 ms, field of view (FoV) = 19.2 x 19.2 mm², matrix size = 192 x 192, resolution = 0.1 x 0.1 x 0.5 mm³). Nine contiguous slices were acquired in healthy mice (TR = 1800 ms, TE = 54 ms, FoV = 20 x 20 mm², matrix size = 256 x 256, resolution = 0.078 x 0.078 x 1 mm³).

#### Volumetric MRI and MRE in humans

Imaging was performed on a clinical 3T MRI scanner (Magnetom Lumina, Siemens, Erlangen, Germany) using a 32-channel head coil. Axial T1-weighted (T1w) images were acquired in a central slap through the brain using the scanner's auto align function and a magnetization-prepared rapid acquisition gradient echo (MPRAGE) sequence (TR = 2300 ms, TE = 2.27 ms, FoV =  $192 \times 192 \text{ mm}^2$  and matrix size =  $128 \times 128$ , resolution =  $1.5 \times 1.5 \times 2 \text{ mm}^3$ ). In glioma patients, either 15 or 36 slices were acquired to minimize acquisition time, depending on the patient's

compliance. In healthy subjects, the full brain was covered with 256 slices and a resolution of 1  $\times$  1  $\times$  1 mm<sup>3</sup>.

Multifrequency MRE was performed using a single-shot, spin-echo, echo-planar imaging sequence with four consecutively applied drive frequencies of 20, 25, 30, and 40 Hz. The central MRE slice was aligned with the central slice of the T1w image block. As shown in Figure 1A, each subject's head was positioned on 3D-printed air cushions $^{52}$ . Three orthogonal wave displacement components were encoded using a single-cycle, flow-compensated motion-encoding gradient (amplitude = 34 mT/m, duration = 28 ms). Corresponding to the T1w scans, either 15 or 36 contiguous transverse slices were acquired depending on patient comfort level while 9 slices were acquired in healthy subjects using the same sequence (TR = 4700 ms, TE = 70 ms, FoV = 202 × 202 mm² and matrix size = 128 × 128, resolution = 1.603 x 1.603 x 2 mm³)

#### Data postprocessing

The data postprocessing workflow is presented in Figure 5C. Multifrequency MRE inversion was performed using Matlab 24.2.0.2833386 (R2024b), Update 4 (MathWorks, Natick, MA). Statistical analysis was done in R version 4.4.2. All other postprocessing steps were implemented in Python (Python 3.10.13, Python Software Foundation, USA).

#### Shear modulus calculation

Shear wave speed (SWS) maps for both mice and human subjects were generated using the k wave-number-based multifrequency dual elasto-visco (k-MDEV) inversion method, which is publicly accessible at https://bioqic-apps.charite.de $^{53}$  and outlined in Figure 5B. Briefly, the raw phase data was unwrapped, followed by a temporal Fourier transform to extract the fundamental of angular drive frequency  $\omega$  in each voxel. The resulting complex-valued wave images were then directionally filtered along the main axes and diagonal axes, resulting in a set of  $8\times3\times4$  shear wave images per slice,  $u_{dcf}$ , corresponding to eight directions (d), three wavefield components (c) and three drive frequencies (f) $^{53,54}$ . Spatial phase gradients were then used to derive wave numbers

$$k_{dcf} = \|\nabla \arg(u_{dcf})\|. \tag{1}$$

where  $\|\cdot\|$  denotes the Euclidean norm,  $\nabla$  is the gradient operator, and arg extracts the phase of a complex number. The resulting  $8\times3\times4\,k_{dcf}$  images were compounded into a single SWS map after weighting reciprocal wave numbers with weights  $W=|u_{dcf}|^2$  and averaging them across components, directions, and N frequencies:

$$SWS = \frac{N}{\sum_{f=1}^{N} \frac{1}{SWS_f}} \text{ where } SWS_f = \frac{\omega \sum_{d} \sum_{c} W}{\sum_{d} \sum_{c} k_{dcf} W}$$
 (2)

Finally, SWS maps were converted into shear modulus  $\mu$  maps by assuming a unit tissue mass density  $\rho$  of 1000 kg/m³  $^{55}$  according to

$$\mu = SWS^2 \rho. \tag{3}$$

Tissue values were distinguished from fluid regions by thresholding SWS maps with 1 m/s<sup>55, 56</sup>.

#### Registration

First image pixel of the skull were removed on human T1w images using SynthStrip<sup>57</sup> - a deep-learning-based tool to strip non-brain tissues from MRI scans for subsequent analysis. Skull pixels in T2w brain images of mice were removed using RS2-NET<sup>58</sup>. The images were then resampled to an isotropic voxel resolution of 1 mm<sup>3</sup> and normalized into an intensity range between 0 and 1. Next, rigid and affine registrations were performed, using ANTs<sup>59</sup> to align anatomical structures. Finally, diffeomorphic deformable image registration was applied using

TransMorph<sup>60</sup>. A publicly available, pretrained model was used for human subjects<sup>60</sup>. For mouse data, a separate network with the same underlying architecture was trained on 350 mouse datasets. Human images were registered to the MNI ICBM Human Brain Atlas<sup>48</sup> and mouse brains to the DSURQE Mouse Brain Atlas<sup>49</sup>. Additionally, mouse brains imaged at time point 22 days were registered to their corresponding images acquired at time point 13 days.

#### Strain

The following notations were used for volumetric and shear strain. Computed displacement field  $\mathbf{u}(\mathbf{r})$  maps undeformed coordinates  $\mathbf{r}$  onto deformed coordinates  $\mathbf{r}'$ :

$$\mathbf{r}' = \mathbf{r} + \mathbf{u}(\mathbf{r}). \tag{4}$$

The magnitude of displacement is defined by the Euclidean norm

$$D(\mathbf{u}(\mathbf{r})) = \|\mathbf{u}(\mathbf{r})\| = \sqrt{u_1^2 + u_2^2 + u_3^2}$$
 (5)

The finite strain (large deformation) induced by the growing tumor was defined by the Green-Lagrange strain tensor based on the deformation gradient  $\mathbf{F} = \frac{\partial \mathbf{r'}}{\partial \mathbf{r}} = \mathbf{I} + \nabla \mathbf{u}$ :

$$\mathbf{E} = \frac{1}{2} (\mathbf{F}^T \mathbf{F} - \mathbf{I}) = \frac{1}{2} (\nabla \mathbf{u} + \nabla \mathbf{u}^T + (\nabla \mathbf{u})^T \nabla \mathbf{u}), \tag{6}$$

where **I** is the identity matrix and  $\mathbf{u}^T$  denotes the transpose of  $\mathbf{u}$ . Volumetric strain was defined by the first invariant of the strain tensor **E** and the octahedral shear strain (OSS)<sup>61</sup>, respectively as:

Volumetric strain: 
$$tr(\mathbf{E}) = E_{11} + E_{22} + E_{33}$$
 (7a)

Octahedral Shear strain (OSS):

$$\frac{2}{3}\sqrt{(E_{11}-E_{22})^2+(E_{11}-E_{33})^2+(E_{22}-E_{33})^2+6(E_{12}^2+E_{13}^2+E_{23}^2)}$$
 (7b)

Note, the sign of volumetric strain indicates the direction of deformation with negative strain referring to compression and positive strain expansion. In contrast, OSS has only positive values. Since image registration to the pre-deformed, non-tumoral reference state is not feasible in patients, we used a mouse model of GBM tumors for validation and variability analysis. This enabled us to assess differences between atlas-based and individual reference-based registrations and to thus identify potential biases in strain estimation.

#### Regional Analysis

To account for interindividual anatomical variability, regional deformation analysis was performed. Displacement field magnitude according to equation (5) was computed within a cohort of healthy controls. The 95<sup>th</sup> percentile was used as the threshold below which deformation was considered nonsignificant in patients. Conversely, regions above this threshold were classified as abnormally deformed regions and were observed around tumors (Figure 5D). To mitigate high displacement magnitudes due to boundary artifacts, we restricted analysis to a brain mask eroded by five voxels and disregarded regions smaller than 10 voxels. Deviations of individual brain anatomy from normative brain atlas anatomy were accounted for by subtracting group-mean healthy volumetric strain  $\overline{tr(E)_0}$  and mean healthy  $\overline{OSS_0}$  from each patient's strain:

$$\overline{tr(\mathbf{E})} = tr(\mathbf{E})_{alioma} - \overline{tr(\mathbf{E})_0}, \tag{8a}$$

$$\overline{OSS} = OSS_{alioma} - \overline{OSS_0}.$$
 (8b)

#### Excess solid stress

For isotropic elastic materials, Hooke's law relates strain to stress. However, when dealing with finite (medium-sized) deformations, we must consider geometric nonlinear effects, and the infinitesimal strain tensor used in Hooke's law is replaced by the nonlinear Green-Lagrange strain tensor  $\bf E$ , as defined in equation (6). The resulting constitutive law defines the Cauchy stress tensor

$$\mathbf{\sigma} = \lambda \operatorname{tr}(\mathbf{E})\mathbf{I} + 2\mu \mathbf{E} \tag{9}$$

with  $\lambda$  and  $\mu$  denoting the first and second Lamé's parameter, respectively.  $\mu$  is also referred to as the shear modulus. Volumetric stress, also known as pressure, is given by

$$\sigma_{vol} = -\frac{1}{3}tr(\mathbf{\sigma}) = -(\frac{2\nu}{1-2\nu} + \frac{2}{3})\mu \cdot tr(\mathbf{E}). \tag{10}$$

In this equation,  $\lambda$  was substituted with  $\frac{2\nu\mu}{1-2\nu}$ , where  $\nu$  is Poisson's ratio – a measure of compressibility, which is 0.5 for incompressible materials like water. Because brain tissue has a high water content of 70–80%, it is generally considered nearly incompressible, resulting in values of  $\nu$  close to  $0.5^{62}$ . However, solid tumors deform surrounding tissue over longer time scales, inducing fluid drainage, tissue atrophy, and necrosis. As a result, mass conservation is violated, leading to volumetric changes in peritumoral areas. Consequently, tumor-deformed tissue may exhibit substantially increased compressibility, with reported Poisson's ratios on the order of  $0.4^{32,\,63-65}$ . Unlike volumetric stress, which is pressure, shear stress is associated with volume-conserving deformations, represented by the off-diagonal elements of the Green–Lagrange strain tensor E. These elements can be combined into the shear-strain invariant, OSS<sup>61</sup>, as defined in Equation (7b), which quantifies the maximum shear strain in a deformed solid. Analogously, we define maximum shear stress as

$$\sigma_{shear} = 2\mu \cdot OSS. \tag{11}$$

Tumor-induced solid stress,  $\sigma=\sigma_{vol}+\sigma_{shear}$ , acts on surrounding tissue over extended time periods, leading to tissue damage and remodeling. While volumetric changes are reflected in the Lamé parameter  $\lambda$  and Poisson's ratio  $\nu$ , structural tissue changes are reflected in shear modulus  $\mu$ . Since structural changes, such as tissue degradation associated with softening, are potentially crucial for prognosis and outcome, we introduce the differential shear modulus  $\Delta\mu=\mu_0-\mu_1$ , where  $\mu_0$  and  $\mu_1$  denote the shear moduli before and after deformation, respectively. In clinical practice, the reference state of  $\mu_0$  before deformation is unknown. As an approximation, we assume that apparently unaffected brain tissue in patients with glioma represents the predeformation state with shear modulus  $\mu_0$ , while  $\mu_1$  corresponds to the peritumoral region deformed by the tumor. Then, the product of differential shear modulus  $\Delta\mu=\mu_0-\mu_1$  (reflecting the mechanical consequence) and strain (reflecting the mechanical cause) provides a quantitative measure of excess solid stress  $\Sigma_{vol}$  and  $\Sigma_{shear}$  corresponding to the type of deformation, i.e., volumetric (vol) or shear:

$$\Sigma_{\text{vol}} = \Delta \mu \cdot tr(\mathbf{E}) \tag{12a}$$

$$\Sigma_{\rm shear} = \Delta \mu \cdot OSS \tag{12b}$$

#### Statistical Analysis

Nonparametric tests were used for all statistical analyses to avoid bias induced by the small sample size<sup>66, 67</sup>. A Wilcoxon signed-rank test was used to test for differences in volumetric strain, OSS, SWS, and stress between different regions in the brain. A Wilcoxon-Mann-Whitney test was applied to test for differences in volumetric strain, OSS, and SWS between glioma patients and

healthy subjects. The relationship of strain and stiffness as well as excess solid stress and survival was determined using linear regression. Pearson's linear correlation coefficient R along with p-values compared to the constant model are reported. Group values are reported as mean and standard deviation (SD). p-values <0.05 were considered significant.

## **Data Availability Statement**

The data that supports the findings of this study, except clinical imaging data, are available from the corresponding author upon request. Summary statistics and region average values for all subjects are provided in the supplementary material.

# Acknowledgements

Support from the German Research Foundation (DFG): CRC1340 Matrix in- ision, CRC1540 EBM, GRK2260 BIOQIC and FOR5628, is gratefully acknowledged. The authors thank the Scientific Computing Unit of the IT Division of *Charité – Universitätsmedizin Berlin* for providing computational resources that have contributed to the research results reported in this paper. Dr. Shahryari is a participant in the BIH Charité Junior Digital Clinician Scientist Program funded by the Charité – Universitätsmedizin Berlin, and the Berlin Institute of Health at Charité (BIH).

# **Declaration of interest**

The authors declare that they have no known competing financial interests or personal relationships that might have influenced the work reported in this paper.

# References

- 1. Ostrom, Q.T. et al. CBTRUS statistical report: Primary brain and central nervous system tumors diagnosed in the United States in 2006-2010. *Neuro Oncol* **15 Suppl 2**, ii1-56 (2013).
- 2. Krex, D. et al. Long-term survival with glioblastoma multiforme. *Brain* **130**, 2596-2606 (2007).
- 3. Efremov, L., Abera, S.F., Bedir, A., Vordermark, D. & Medenwald, D. Patterns of glioblastoma treatment and survival over a 16-years period: pooled data from the German Cancer Registries. *J Cancer Res Clin Oncol* **147**, 3381-3390 (2021).
- 4. van den Bent, M.J. et al. Primary brain tumours in adults. *Lancet* **402**, 1564-1579 (2023).
- 5. Salvalaggio, A., Pini, L., Bertoldo, A. & Corbetta, M. Glioblastoma and brain connectivity: the need for a paradigm shift. *Lancet Neurol* **23**, 740-748 (2024).
- 6. Miroshnikova, Y.A. et al. Tissue mechanics promote IDH1-dependent HIF1 alphatenascin C feedback to regulate glioblastoma aggression. *Nature Cell Biology* **18**, 1336-+ (2016).
- 7. Sun, Y. et al. Brain-wide neuronal circuit connectome of human glioblastoma. *Nature* **641**, 222-231 (2025).
- 8. Kim, Y. & Kumar, S. CD44-mediated adhesion to hyaluronic acid contributes to mechanosensing and invasive motility. *Mol Cancer Res* **12**, 1416-1429 (2014).
- 9. Wang, X. et al. Mechanical nanosurgery of chemoresistant glioblastoma using magnetically controlled carbon nanotubes. *Sci Adv* **9**, eade5321 (2023).
- 10. Streibel, Y. et al. Tumor biomechanics as a novel imaging biomarker to assess response to immunotherapy in a murine glioma model. *Sci Rep* **14**, 15613 (2024).
- 11. Sack, I. Magnetic resonance elastography from fundamental soft-tissue mechanics to diagnostic imaging. *Nature Reviews Physics* **5**, 25-42 (2023).

- 12. Streitberger, K.J. et al. High-resolution mechanical imaging of glioblastoma by multifrequency magnetic resonance elastography. *PLoS One* **9**, e110588 (2014).
- 13. Reiss-Zimmermann, M. et al. High Resolution Imaging of Viscoelastic Properties of Intracranial Tumours by Multi-Frequency Magnetic Resonance Elastography. *Clin Neuroradiol* **25**, 371-378 (2015).
- 14. Bunevicius, A., Schregel, K., Sinkus, R., Golby, A. & Patz, S. REVIEW: MR elastography of brain tumors. *Neuroimage Clin* **25**, 102109 (2020).
- 15. Flogstad Svensson, S. et al. Decreased tissue stiffness in glioblastoma by MR elastography is associated with increased cerebral blood flow. *Eur J Radiol* **147**, 110136 (2022).
- 16. Streitberger, K.J. et al. How tissue fluidity influences brain tumor progression. *Proc Natl Acad Sci U S A* **117**, 128-134 (2020).
- 17. Sauer, F. et al. Changes in Tissue Fluidity Predict Tumor Aggressiveness In Vivo. *Adv Sci* (Weinh) **10**, e2303523 (2023).
- 18. Prasanna, P. et al. Mass Effect Deformation Heterogeneity (MEDH) on Gadolinium-contrast T1-weighted MRI is associated with decreased survival in patients with right cerebral hemisphere Glioblastoma: A feasibility study. *Sci Rep-Uk* **9** (2019).
- 19. Ismail, M. et al. Radiomic Deformation and Textural Heterogeneity (R-DepTH) Descriptor to Characterize Tumor Field Effect: Application to Survival Prediction in Glioblastoma. *Ieee T Med Imaging* **41**, 1764-1777 (2022).
- 20. Jain, R.K., Martin, J.D. & Stylianopoulos, T. The role of mechanical forces in tumor growth and therapy. *Annu Rev Biomed Eng* **16**, 321-346 (2014).
- 21. Pogoda, K. et al. Compression stiffening of brain and its effect on mechanosensing by glioma cells. *New J Phys* **16**, 075002 (2014).
- 22. Cai, G. et al. Compressive stress drives adhesion-dependent unjamming transitions in breast cancer cell migration. *Front Cell Dev Biol* **10**, 933042 (2022).
- 23. Hohmann, U. et al. Jamming Transitions in Astrocytes and Glioblastoma Are Induced by Cell Density and Tension. *Cells* **12**, 29 (2022).
- 24. Seano, G. et al. Solid stress in brain tumours causes neuronal loss and neurological dysfunction and can be reversed by lithium. *Nat Biomed Eng* **3**, 230-245 (2019).
- 25. Nia, H.D.T., Munn, L.L. & Jain, R.K. CANCER Physical traits of cancer. *Science* **370**, 546 (2020).
- 26. Nia, H.T. et al. Solid stress and elastic energy as measures of tumour mechanopathology. *Nat Biomed Eng* **1**, 0004 (2016).
- 27. Nia, H.T. et al. Quantifying solid stress and elastic energy from excised or in situ tumors. *Nat Protoc* **13**, 1091-1105 (2018).
- 28. Page, G. et al. Tumor Solid Stress: Assessment with MR Elastography under Compression of Patient-Derived Hepatocellular Carcinomas and Cholangiocarcinomas Xenografted in Mice. *Cancers (Basel)* **13**, 1891 (2021).
- 29. Jaitner, N. et al. Noninvasive assessment of portal pressure by combined measurement of volumetric strain and stiffness of in vivo human liver. *Acta Biomaterialia* **197**, 312-325 (2025).
- 30. Pepin, K.M. et al. MR Elastography Analysis of Glioma Stiffness and IDH1-Mutation Status. *AJNR Am J Neuroradiol* **39**, 31-36 (2018).
- 31. Janas, A. et al. In vivo characterization of brain tumor biomechanics: magnetic resonance elastography in intracranial B16 melanoma and GL261 glioma mouse models. *Front Oncol* **14**, 1402578 (2024).
- 32. Moran, R., Smith, J.H. & Garcia, J.J. Fitted hyperelastic parameters for Human brain tissue from reported tension, compression, and shear tests. *J Biomech* **47**, 3762-3766 (2014).
- 33. Huber, W., Poeck, K., Weniger, D. & Willmes, K. Aachener Aphasie-Test (AAT). (Verlag für Psychologie Dr. C.J. Hogrefe, 1983).

- 34. Bergs, J., Morr, A.S., Silva, R.V., Infante-Duarte, C. & Sack, I. The Networking Brain: How Extracellular Matrix, Cellular Networks, and Vasculature Shape the In Vivo Mechanical Properties of the Brain. *Adv Sci (Weinh)* **11**, e2402338 (2024).
- 35. Ballestin, A., Armocida, D., Ribecco, V. & Seano, G. Peritumoral brain zone in glioblastoma: biological, clinical and mechanical features. *Front Immunol* **15**, 1347877 (2024).
- 36. Drumm, M.R. et al. Extensive brainstem infiltration, not mass effect, is a common feature of end-stage cerebral glioblastomas. *Neuro Oncol* **22**, 470-479 (2020).
- 37. Lacroix, M. et al. A multivariate analysis of 416 patients with glioblastoma multiforme: prognosis, extent of resection, and survival. *J Neurosurg* **95**, 190-198 (2001).
- 38. Steed, T.C. et al. Quantification of glioblastoma mass effect by lateral ventricle displacement. *Sci Rep* **8**, 2827 (2018).
- 39. Wang, C. et al. Matrix Stiffness Modulates Patient-Derived Glioblastoma Cell Fates in Three-Dimensional Hydrogels. *Tissue Eng Part A* **27**, 390-401 (2021).
- 40. Streitberger, K.J. et al. In vivo viscoelastic properties of the brain in normal pressure hydrocephalus. *NMR Biomed* **24**, 385–392 (2011).
- 41. Agarwal, S., Sane, R., Oberoi, R., Ohlfest, J.R. & Elmquist, W.F. Delivery of molecularly targeted therapy to malignant glioma, a disease of the whole brain. *Expert Rev Mol Med* 13, e17 (2011).
- 42. Fierstra, J. et al. Diffuse gliomas exhibit whole brain impaired cerebrovascular reactivity. *Magn Reson Imaging* **45**, 78-83 (2018).
- 43. Claes, A., Idema, A.J. & Wesseling, P. Diffuse glioma growth: a guerilla war. *Acta Neuropathol* **114**, 443-458 (2007).
- 44. Sack, I., Beierbach, B., Hamhaber, U., Klatt, D. & Braun, J. Non-invasive measurement of brain viscoelasticity using magnetic resonance elastography. *NMR Biomed* **21**, 265-271 (2008).
- 45. Guo, J. et al. Towards an elastographic atlas of brain anatomy. *PLoS One* **8**, e71807 (2013).
- 46. Nia, H.T. et al. Solid stress estimations via intraoperative 3D navigation in patients with brain tumors. *Clin Cancer Res* (2025).
- 47. Ranft, J. et al. Fluidization of tissues by cell division and apoptosis. *Proc Natl Acad Sci U S A* **107**, 20863-20868 (2010).
- 48. Mazziotta, J. et al. A four-dimensional probabilistic atlas of the human brain. *J Am Med Inform Assoc* **8**, 401-430 (2001).
- 49. Dorr, A.E., Lerch, J.P., Spring, S., Kabani, N. & Henkelman, R.M. High resolution three-dimensional brain atlas using an average magnetic resonance image of 40 adult C57BI/6J mice. *Neuroimage* **42**, 60-69 (2008).
- 50. Guo, J. et al. Brain maturation is associated with increasing tissue stiffness and decreasing tissue fluidity. *Acta Biomaterialia* **99**, 433-442 (2019).
- 51. Jelgersma, C. et al. Establishment and Validation of CyberKnife Irradiation in a Syngeneic Glioblastoma Mouse Model. *Cancers (Basel)* **13**, 3416 (2021).
- 52. Herthum, H. et al. Cerebral tomoelastography based on multifrequency MR elastography in two and three dimensions. *Front Bioeng Biotechnol* **10**, 1056131 (2022).
- 53. Meyer, T. et al. Comparison of inversion methods in MR elastography: An open-access pipeline for processing multifrequency shear-wave data and demonstration in a phantom, human kidneys, and brain. *Magn Reson Med* **88**, 1840-1850 (2022).
- 54. Tzschatzsch, H. et al. Tomoelastography by multifrequency wave number recovery from time-harmonic propagating shear waves. *Medical Image Analysis* **30**, 1-10 (2016).
- 55. Manduca, A. et al. MR elastography: Principles, guidelines, and terminology. *Magn Reson Med* **85**, 2377-2390 (2021).
- 56. Klemmer Chandia, S. et al. Multimodal assessment of brain stiffness variation in healthy subjects using magnetic resonance elastography and ultrasound time-harmonic elastography. *Sci Rep* **14**, 28580 (2024).

- 57. Hoopes, A., Mora, J.S., Dalca, A.V., Fischl, B. & Hoffmann, M. SynthStrip: skull-stripping for any brain image. *Neuroimage* **260**, 119474 (2022).
- 58. Lin, Y. et al. RS2-Net: An end-to-end deep learning framework for rodent skull stripping in multi-center brain MRI. *NeuroImage* **298**, 120769 (2024).
- 59. Avants, B.B. et al. A reproducible evaluation of ANTs similarity metric performance in brain image registration. *Neuroimage* **54**, 2033-2044 (2011).
- 60. Chen, J. et al. TransMorph: Transformer for unsupervised medical image registration. *Med Image Anal* **82**, 102615 (2022).
- 61. McGarry, M.D.J. et al. An octahedral shear strain-based measure of SNR for 3D MR elastography. *Physics in Medicine and Biology* **56**, N153-N164 (2011).
- 62. Whittall, K.P. et al. In vivo measurement of T2 distributions and water contents in normal human brain. *Magn Reson Med* **37**, 34-43 (1997).
- 63. Soza, G. et al. Determination of the elasticity parameters of brain tissue with combined simulation and registration. *Int J Med Robot* **1**, 87-95 (2005).
- 64. Laksari, K., Shafieian, M. & Darvish, K. Constitutive model for brain tissue under finite compression. *J Biomech* **45**, 642-646 (2012).
- 65. Eskandari, F., Rahmani, Z. & Shafieian, M. The effect of large deformation on Poisson's ratio of brain white matter: An experimental study. *Proc Inst Mech Eng H* **235**, 401-407 (2021).
- 66. Ghasemi, A. & Zahediasl, S. Normality tests for statistical analysis: a guide for non-statisticians. *Int J Endocrinol Metab* **10**, 486-489 (2012).
- 67. Pereira, D.G., Afonso, A. & Medeiros, F.M. Overview of Friedman's Test and Post-hoc Analysis. *Commun Stat-Simul C* **44**, 2636-2653 (2015).